

Fast thermal desorption spectroscopy study of H/D isotopic exchange reaction in polycrystalline ice near its melting point

Haiping Lu, Stephanie A. McCartney, and Vlad Sadtschenko^{a)}

Department of Chemistry, The George Washington University, Washington, DC 20052, USA

(Received 24 October 2006; accepted 24 August 2007; published online 8 November 2007)

Using fast thermal desorption spectroscopy, a novel technique developed in our laboratory, we investigated the kinetics of H/D isotopic exchange in 3 μm thick polycrystalline H_2O ice films containing D_2O layers at thicknesses ranging from 10 to 300 nm at a temperature of -2.0 ± 1.5 °C. According to our results over the duration of a typical fast thermal desorption experiment (3–4 ms), the isotopic exchange is confined to a 50 ± 10 nm wide reaction zone located at the boundary between polycrystalline H_2O and D_2O ice. Combining these data with a theoretical analysis of the diffusion in polycrystalline medium, we establish the range of possible values for water self-diffusion coefficients and the grain boundary widths characteristic of our ice samples. Our analysis shows that for the grain boundary width on the order of a few nanometers, the diffusivity of D_2O along the grain boundaries must be at least two orders of magnitude lower than that in bulk water at the same temperature. Based on these results, we argue that, in the limit of low concentrations of impurities, polycrystalline ice does not undergo grain boundary premelting at temperatures up to -2 °C. © 2007 American Institute of Physics. [DOI: 10.1063/1.2786101]

I. INTRODUCTION

In polycrystalline solids, the grain boundaries often provide efficient channels for the transport of various chemical species and determine the mechanical and electrical properties of the materials. Therefore, fundamental studies of condensed phase phenomena within the grain boundaries are of significant interest to many applied fields of science. For example, the grain boundaries of polycrystalline ice play a crucial role in a variety of environmentally relevant processes and technologies, such as frost heave, glacier motion, growth and decay of sea ice, dynamics of polar ice caps, chemical processing of pollutants in the atmosphere, water purification and desalination by freezing, and analysis of ice core climate proxies.^{1–22}

Due to the extremely low solubility of most molecular species in single crystal ice samples, the grain boundaries (GB's) in polycrystalline ice samples serve as the primary storage and reaction sites for chemical impurities. Therefore, an understanding of the bulk reactivity in polycrystalline ice requires extensive information on the properties of the condensed aqueous phase confined at the GB's. Such information includes the GB dimensions at various temperatures, the transport properties of GB's i.e., the diffusivity of water and other chemical species along the GB's, and the reactivity of water and other chemical species confined to microscopic dimensions characteristic of grain boundaries. Although the surface and bulk properties of single crystal ice have been the subject of many past experimental studies, the GB phenomena in ice have remained relatively unexplored.^{23–28} Im-

mediately below, we cite several examples of outstanding questions on properties of polycrystalline ice, which still await definite answers.

To begin, there have been only a few studies of the transport phenomena along GB's in polycrystalline ice. Kunh and Thürkauf²⁹ employed isotopic variants of water, HDO and H_2O^{18} , as tracers to measure the self-diffusivity of water in polycrystalline ice near its melting point. The results showed that the effective diffusion coefficients of HDO and H_2O^{18} in polycrystalline ice were both on the order of 10^{-14} m^2/s at -1.8 °C, which is approximately an order of magnitude higher than that for ice single crystals at the same temperature. While emphasizing the fact that the diffusion of water is indeed rapid in polycrystalline ice samples, these, as well as later studies,^{30,31} did not explicitly address molecular transport at the grain boundaries and related defects.

The lack of fundamental understanding of the transport and other properties of aqueous phase confined at the GB's hinders the progress in many relevant applied fields. For example, Johnsen *et al.* determined that the water self-diffusion coefficients in naturally occurring ice from Greenland were much higher than those in pristine single crystal ice.³² As suggested by Nye, this may be due to the formation of quasi-liquid channels at the intersection of GB's, i.e., at the "veins," in the bulk of the polycrystalline ice samples.³³ However, Johnsen *et al.* later demonstrated that the dimensions of such veins would be unrealistically large to account for rapid diffusion.³⁴

The existence of liquid inclusions in the bulk of polycrystalline ice, mentioned above, is a manifestation of the interfacial premelting phenomenon, which consists in the formation of liquid layers at various interfaces of crystalline material at temperatures significantly lower than its bulk melting point.^{35–39} Although premelting has been observed at

^{a)} Author to whom correspondence should be addressed. Tel.: 202-994-6155. Electronic mail: vlad@gwu.edu

ice surfaces and the interface between ice and other solids, there is no experimental evidence that premelting takes place at the GB's in *pure* ice. Therefore, the following fundamental question arises: what is the extent of grain boundary premelting in the limit of low impurity concentration?

In the absence of experimental studies on GB premelting, one has to rely exclusively upon theoretical results. For example, Benatov and Wettlaufer came to the conclusion that, in the limit of extremely low concentrations of impurities, GB premelting is virtually nonexistent even at temperatures a few millikelvins below the bulk melting point. Furthermore, according to their analysis, the extent of premelting, i.e., the width of the liquid layer at the GB, may demonstrate a complex dependence on the concentration and nature of the impurities.³⁹ For instance, the width of the GB's was predicted to undergo a radical increase (up to four orders of magnitude) at some "critical" temperature, which is a function of impurity type and concentration. This possible scenario of premelting was termed "abrupt grain boundary melting." The results of this intriguing theoretical study have yet to be substantiated by experiment.

Experimental studies on the chemical and physical phenomena, which take place at the GB's, are difficult. Naturally occurring ice samples, as well as those grown in the laboratory, are usually characterized by a relatively large average grain size, which makes it difficult to distinguish between processes at the grain boundaries and in the crystallites. Furthermore, only a few experimental techniques allow easy access to phenomena within the GB's. While the free surface of ice can be interrogated directly using a variety of spectroscopic approaches, such studies are virtually impossible in the case of interfaces within the ice bulk. For example, application of infrared spectroscopic methods to studies of GB phenomena requires complicated optical arrangements and the use of extremely thin polycrystalline ice films.⁴⁰

Motivated by fundamental and applied significance of grain boundary phenomena in polycrystalline ice, we recently used fast thermal desorption spectroscopy (FTDS) to study diffusion and reactions of various chemical species at the GB's. In particular, we conducted the first real-time investigation of the diffusion-limited kinetics of the H/D exchange reaction in polycrystalline ice samples with extremely fine (<30 nm in diameter) grains at -2 °C. As we will demonstrate in the following sections of this article, our novel experimental approach is uniquely suited for studies of chemical and physical phenomena at grain boundaries in polycrystalline ice near its melting point and makes it possible to gain insights into phase transitions, chemical transport, and reactivity at these complex and important aqueous interfaces.

II. EXPERIMENT

A. Overview

A detailed description of the FTDS apparatus and standard experimental procedures can be found elsewhere;^{21,41} therefore, only a brief description is provided in this section. As shown in Fig. 1(a), ice films are grown on the surface of a tungsten filament (10 μm in diameter, 2 cm long), which is

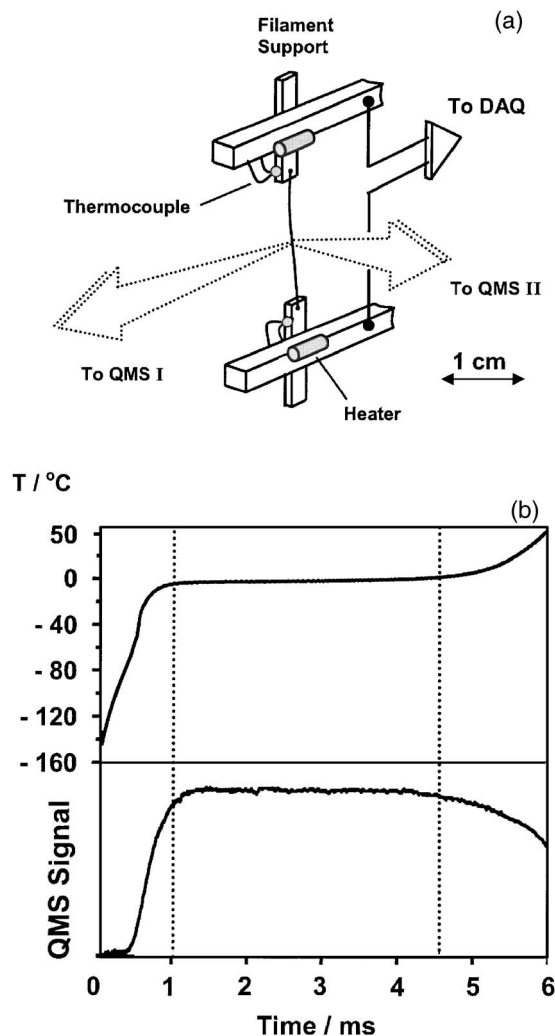


FIG. 1. (a) The essentials of the fast thermal desorption spectroscopy (FTDS). Polycrystalline ice films are grown on the surface of a tungsten filament, which is 10 μm in diameter and 2 cm long. The filament is spot welded to two supports, which are in thermal contact with a liquid-nitrogen (LN)-cooled heat sink. During ice film deposition, the temperature of the entire filament assembly can be varied from -160 to -100 °C by balancing heat flux from resistive heaters against heat loss to the LN sink. The temperature of the filament supports is monitored by two T-type thermocouples. Rapid vaporization of the film near 0 °C is initiated by a current pulse from a data acquisition (DAQ) system. The fluxes of vaporization/reaction products can be monitored by either of two quadrupole mass spectrometers (QMSs) or a fast ionization gauge (FIG). The current through the filament, applied voltage, and the FIG and QMS signals are recorded by the DAQ system every 4 μs . (b) The essential data obtained in a FTDS experiment. Upper panel: The temperature of the filament as a function of time. The temperature is calculated from resistance data. Lower panel: The overall vaporization flux from the filament as a function of time as measured with the FIG.

spot welded to the supports of the filament assembly. The supports, while in thermal contact with the liquid-nitrogen-cooled heat sink, are electrically isolated from the rest of the apparatus. The filament assembly includes a thermal control system capable of maintaining the filament supports at temperatures ranging from -160 to -100 °C. The assembly is surrounded by cryogenic shields (not shown) and positioned in a vacuum chamber pumped with a 2500 l s^{-1} Varian diffusion pump. The chamber is maintained at pressures below 3×10^{-7} Torr during all stages of FTDS experiments.

Water vapors (H_2O^{16} , H_2O^{18} , and D_2O) are delivered from the vapor source to the filament via an array of effusive dosers, which consist of 12 stainless steel tubes with an 1/8 in. diameter. The dosers are equally spaced around the filament at a distance of approximately 5 cm from its center [not shown in Fig. 1(a)]. The intersecting vapor beams from the dosers lead to the formation of a relatively dense water vapor cloud around the tungsten filament, and thus facilitates the deposition of uniform ice films with a neat cylindrical geometry and thickness of up to 4000 nm at rates from 1 to 50 nm s⁻¹.

After deposition, rapid, nearly *isothermal* desorption of the film is initiated by applying a 2–5 V potential difference across the filament. In the course of the entire FTDS experiment, the voltage across the filament and the current through the filament are recorded every 4 μs by a custom designed data acquisition system. The effective resistance values are calculated from current and voltage data according to Ohm's law. The temperature is then calculated from the resistance data using the temperature coefficient of electrical resistivity of tungsten (0.0045 °C⁻¹). A calibration procedure, based on the melting of micrometer thick polycrystalline ice films, was routinely performed to ensure the ± 1.5 °C overall accuracy of filament temperature measurements.^{21,41}

During rapid desorption of the film, the flux of vaporization products are analyzed simultaneously with three types of detectors:

- (1) A fast ionization gauge (FIG) is used to monitor the overall vaporization kinetics of the films. The FIG is essentially a fast Bayard-Alpert ionization gauge with a response time to local pressure variations of less than 3 μs .²¹ The FIG is positioned 6 cm away from the filament behind a centimeter-wide slit cut between cryogenic shields.
- (2) The vaporization products are also analyzed with a quadrupole mass spectrometer (QMS) positioned approximately 10 cm away from the filament (QMS-1). The QMS-1 is a modified residual gas analyzer (RGA 300, Stanford Research Instruments), which is placed inside a differentially pumped vacuum chamber. The pumping system of the QMS-1 chamber consists of 150 l s⁻¹ turbomolecular pump, which is backed with a diffusion pump. The pressure inside the QMS-1 chamber is maintained at 10⁻⁸ Torr. The QMS-1 employs a custom designed electron bombardment ionizer, which is cooled with liquid nitrogen. Vaporization products enter the QMS chamber through a 2 mm skimmer, which is situated 4 cm away from the filament.⁴¹
- (3) In selected experiments, the velocity distributions of vaporization products are analyzed with a time-of-flight (TOF) setup, which utilizes a sensitive quadrupole mass spectrometer (QMS-2), and a rotating chopper wheel. The QMS-2 is positioned inside a doubly differentially pumped chamber at approximately 1 m away from the filament.²¹

Figure 1(b) illustrates the typical data obtained in a FTDS experiment. It shows the H_2O flux from the filament and the corresponding temperature of the filament. The H_2O

flux was measured with the QMS-1. As shown in the figure, a rapid rise in the temperature of the filament is followed by the region of relative thermal stability. Indeed, examination of the temperature data, after 1 ms, demonstrates that the temperature of the filament increases by less than 2 °C during the next several milliseconds of the desorption experiment. Achieving a steady-state temperature coincides with the onset of H_2O desorption.

The steady-state vaporization regime can be rationalized in the following way. The heat generated by filament leads to rapid increase in temperature during the initial stage of the experiment. However, at temperatures above -100 °C, resistive heating of the filament is counteracted by cooling due to vaporization. Thus, a dynamic equilibrium is achieved at a temperature where the vaporization rate of ice is sufficiently high so that the power generated by the filament is equal to heat flux from the surface of the filament due to vaporization of the ice film.

Due to cylindrical geometry, the evaporation of ice results in gradual decrease in the surface area of the film during steady-state evaporation. However, a gradual decrease in the surface area also leads to an increase in the temperature of the filament due to lower cooling efficiency. Because of a strong Arrhenius dependence of the vaporization rate on temperatures,²¹ this drift in temperature is less than a few degrees. Although not immediately apparent in Fig. 1, the temperature of the filament indeed increases slowly from -5 to -3 °C during steady-state vaporization of a 3 μm thick ice film. Careful examination of the power, temperature, and vaporization rate data shows, however, that vaporization of the ice samples is consistent with zero-order kinetics.

Observation of zero-order desorption kinetics leads to several important conclusions. First, during isothermal desorption near 0 °C, the ice layer on the surface of the filament is a neat film free of *large* pores or ruptures, i.e., the film covers the entire filament surface.²¹ Second, the temperature gradient *along* the length of the filament is negligible except within a fraction of a millimeter near the ends of the filament.²¹ Finally, since the temperature of the filament does not vary significantly with the film thickness during vaporization, the temperature gradient in the film must be less than a few degrees.²¹

In the past, we also used data from the TOF experiments to characterize thermal gradients across the bulk of vaporizing D_2O ice films.²¹ In these experiments, the temperature of the ice *surface* was determined by fitting Maxwellian distributions to the experimental TOF spectra and was compared to the temperature of the filament derived from resistance measurements. The temperature values obtained by these two methods were equal within the experimental errors (± 3 °C), thus proving that the temperature gradients in FTDS experiments are indeed small.

Mass, thickness, and phase composition of our ice samples were determined by an ultrafast microcalorimetry technique.^{21,41} In these experiments, the combined effective heat capacity of the ice film and the filament was calculated as the ratio of the power generated by the filament to the first time derivative of the temperature. Figure 2 illustrates the

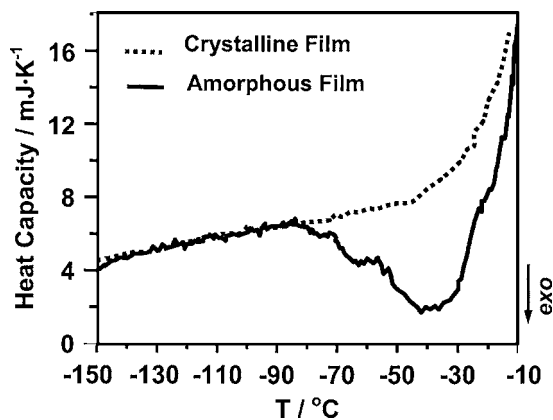


FIG. 2. Typical fast scanning thermograms of amorphous (solid line) and polycrystalline (dashed line) ice samples. In the case of amorphous ice, the thermogram shows multiple exothermal transitions, which we attribute to relaxation of the amorphous ice and its consequent crystallization. The thermograms are inferred from current and voltage data measured during the initial heating of the ice samples in FTDS experiments. The effective heat capacities were calculated as a ratio of the power generated by the filament to the first time derivative of the filament's temperatures.

typical results. The solid line shows the effective heat capacity of the filament with a H_2O film vapor deposited at $-150\text{ }^\circ\text{C}$, and the dotted line shows the effective heat capacity of the filament with a H_2O film vapor deposited at $-150\text{ }^\circ\text{C}$ and then annealed at temperatures near $-10\text{ }^\circ\text{C}$ for a fraction of a millisecond. In the case of the annealed film, the monotonic increase in heat capacity of the filament-film system, i.e., the lack of exothermic transitions characteristic of crystallization, demonstrates that the ice sample is crystalline. However, in the case of the film deposited at $-150\text{ }^\circ\text{C}$, the effective heat capacity shows partially overlapping irreversible exotherms, which we attribute to crystallization of the initially amorphous ice samples.²¹ Assignment of the exotherms shown in Fig. 2 to crystallization of amorphous ice is facilitated by approximately 2 kJ/mol enthalpy release, which is close to previously reported values.^{42,43} These calorimetric experiments also show that noncrystalline ice films always undergo crystallization before steady-state vaporization can occur at temperatures above $-25\text{ }^\circ\text{C}$. Assuming that a crystallized film has the specific heat capacity and density of hexagonal ice, the estimate of the total mass of the film can be obtained by simply dividing the total heat capacity of ice film by the specific heat capacity of hexagonal ice. Using the mass of the ice film and assuming that ice film geometry is close to that of a neat cylinder, we routinely determine the overall thickness of our films with accuracy of $\pm 10\%$.

B. Deposition of ultrathin ice layers

The experiments described in this article required precise control of ice deposition on the surface of the filament. For example, one of the key experimental procedures consisted in systematic adjustment of the thickness of a D_2O ice film sandwiched between $2\text{ }\mu\text{m}$ thick H_2O ice layers from 5 to 300 nm. Although the microcalorimetry technique makes it possible to estimate the dimensions of the micrometer thick film with an accuracy of $\pm 10\%$, it is *not* sufficiently sensitive to detect variations in the film thickness on the

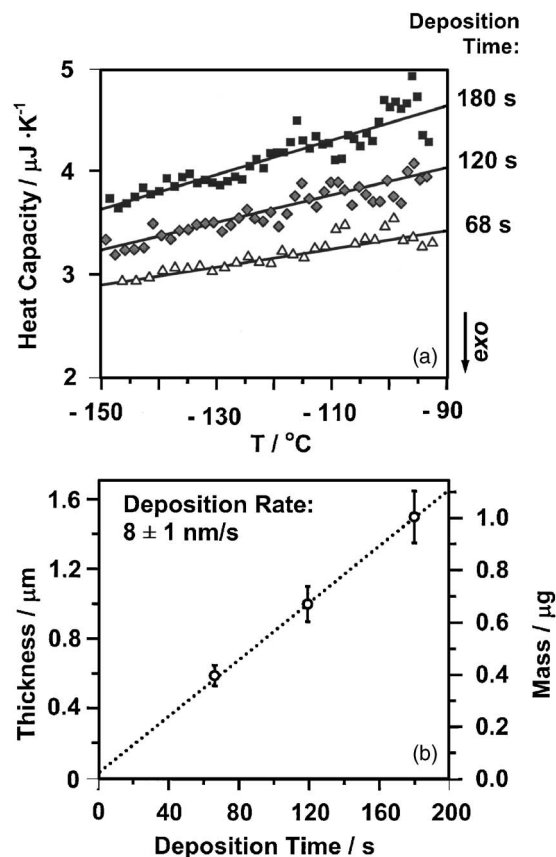


FIG. 3. (a) Variations in the overall heat capacity of the filament with ice deposition time. Longer deposition times result in a greater mass of the ice film on the surface of the filament, thus increasing the total effective heat capacity of the filament-film system. (b) Film mass and thickness as a function of the deposition time. The mass of the film was calculated by dividing the overall heat capacity of the ice sample by the specific heat capacity of hexagonal ice. The film thickness was then calculated assuming that the film had a neat cylindrical geometry during vaporization near $0\text{ }^\circ\text{C}$. The mass and thickness of the ice film increase linearly with deposition time. The linear fit of these data gives the average deposition rate.

nanoscale. Therefore, in the experiments where precise thickness adjustment was required, we had to rely on timed vapor deposition. In other words, we inferred the thicknesses of ultrathin ice layers from the deposition time using a known deposition rate. Immediately below we describe a calibration procedure, which made it possible to control the thickness of ice layers with accuracy down to a few nanometers.

As shown in Fig. 3(a), the heat capacity of the filament-ice system is sensitive to variations in the amount of ice deposited on the filament surface. Indeed, increasing the deposition time results in an increase in the overall effective heat capacity of the filament. Using the heat capacity values in the temperature range from -150 to $-90\text{ }^\circ\text{C}$, we determined the masses of the ice films and the equivalent thicknesses. The plot of these data as a function of the deposition time is shown in Fig. 3(b). As shown in the figure, the thickness of the ice layer increases linearly with deposition time. Thus, the slope of the linear fit gives an average (over time) deposition rate. For example, in the experiments illustrated in Fig. 3, the deposition rate was $8 \pm 1\text{ nm/s}$.

The deposition rate value determined by microcalorim-

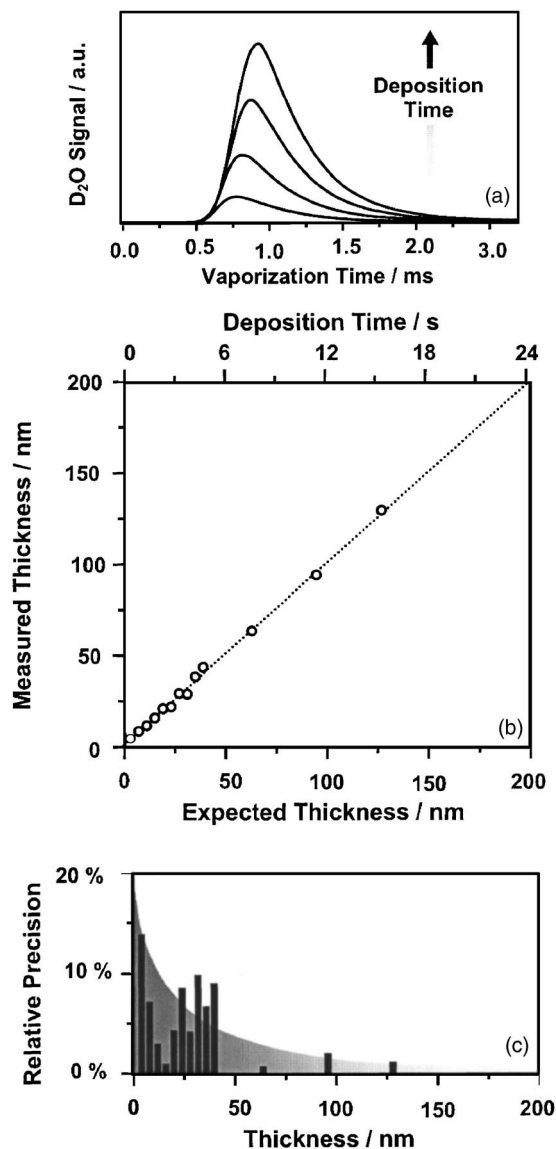


FIG. 4. Typical data used for calibration of the deposition source. (a) Flash desorption spectra of ultrathin ice films. (b) The thicknesses of the ultrathin films as determined by integration of the flash desorption spectra and those calculated as a product of the average deposition rate and time. Excellent correlation between the inferred and measured thickness values signifies a good short term stability of our deposition source. (c) The relative precision of ice deposition, i.e., the relative deviation of predicted thickness from the measured thickness, as a function of deposition time. The data show that random variations in the film thickness, due to deposition source fluctuations, are on the order of 15%, even in the case of ice films which are only 10 nm thick.

entry represents the *average* over deposition times, which were as long as 180 s. However, the deposition times for ultrathin layers were much shorter (down to a fraction of a second). In order to demonstrate that the vapor source employed in our experiments was capable of precise deposition of nanometer-thick ice layers, we developed another calibration procedure which relied on the high sensitivity of our main quadrupole mass spectrometer (QMS-1). The details of these experiments are illustrated in Fig. 4.

Figure 4(a) shows the *flash desorption* spectra of D₂O layers of various thicknesses. The largest spectrum shown in the figure corresponds to a D₂O deposition time of 12 s.

Although not indicated in the plot, the flash desorption spectra give the *absolute* vaporization rate of ultrathin ice films as a function of vaporization time. In other words, the vaporization kinetics measurements depicted in Fig. 4(a) were conducted with a calibrated mass spectrometer. Integration of the flash desorption spectra over the desorption time gives the value of effective thickness of the D₂O ice layer on the surface of the filament. Figure 4(b) compares the thicknesses measured with the calibrated mass spectrometer and those inferred from the parameters of the deposition processes (rate and duration of deposition). The differences between these two values represent the measure of the stability of our vapor source and can be used to determine the precision of the ultrathin layer deposition. As shown in Fig. 4(c), even when the deposition times are less than a second, the resulting layer thickness (a few nanometers) can be reproduced with a relative precision of $\pm 10\%$.

C. Ice film morphology

Before describing the results of our study, we must clarify the meaning of an important experimental parameter, the effective ice film thickness. Most of the experiments described in the following sections of this article begin with deposition of an *amorphous* H₂O/D₂O/H₂O film at -150°C (approximately 120 K). Because the primary objective of our work was to examine the H₂O+D₂O reaction in polycrystalline ice near the melting point, such a low deposition temperature was necessary to minimize the extent of H/D isotopic exchange during deposition. However, rapid deposition of water on a cold substrate at temperatures below 120 K might have resulted in amorphous ice layers characterized by low density, high porosity, and large surface area.⁴²

Considering possible dendritelike morphology of the initially amorphous ice films, the meaning of their effective thicknesses is not immediately clear. We emphasize, however, that the structure and morphology of amorphous films formed during cold deposition have a limited relevance to the discussion of this article. Indeed, as it follows from Fig. 2, initially low-density amorphous ice films always undergo compaction and crystallization at temperatures near -60°C . The resulting polycrystalline ice films are free of large pores and raptures, and demonstrate high-temperature vaporization kinetics, which are indistinguishable from those obtained in experiments with initially crystalline ice.²¹ Thus, the experimentally determined effective thickness of an ice film refers to the thickness of neat polycrystalline ice layer obtained as a result of crystallization and compaction of amorphous (possibly microporous) ice film.

III. RESULTS

A. Fast thermal desorption spectra of D₂O and HDO

Figure 5 shows the fast thermal desorption spectra of D₂O and HDO from 3.3 μm thick H₂O/D₂O/H₂O ice films undergoing vaporization at a near constant temperature of -5°C . The sandwichlike H₂O/D₂O/H₂O films were grown by vapor deposition on the filament's surface at -155°C . The low deposition temperature minimized the reaction be-

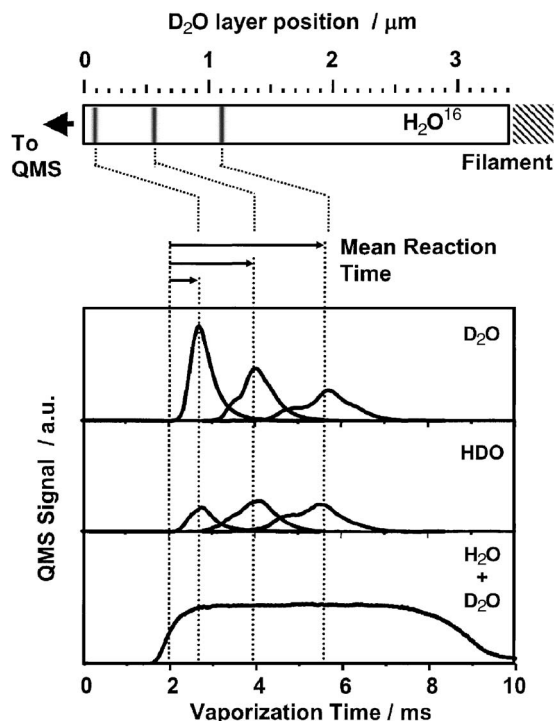


FIG. 5. Fast thermal desorption spectra of D_2O and HDO from a $3 \mu\text{m}$ thick $H_2O/D_2O/H_2O$ film (upper and middle panels) measured at $-5.0 \pm 1.5^\circ\text{C}$. As illustrated in the diagram above, the initial D_2O layer's position was varied from approximately 0.1 to $1.1 \mu\text{m}$ away from the film's surface. The overall desorption kinetics of the film, monitored with the FIG, are shown for comparison (lower panel). The mean reaction time for the H/D isotopic exchange is defined as the mean residence time of D_2O in the bulk of the H_2O film, i.e., the time interval from the onset of H_2O vaporization up to the appearance of the D_2O vaporization peak in the thermal desorption spectrum. Positioning the D_2O layer further away from the surface, i.e., increasing the mean reaction time, results in a gradual decrease of the magnitude of the D_2O peak. The decrease in the D_2O peak is accompanied by an increase in the HDO yield, which signifies the rapid conversion of D_2O into HDO.

tween D_2O and H_2O during film deposition. After the deposition, the films were heated with an average rate in excess of 10^5 K/s to a temperature of -5°C . Based on the thermogram measured during this rapid temperature rise, the initially amorphous $H_2O/D_2O/H_2O$ films underwent a complete crystallization at temperatures near -60°C . The effective thickness of the *crystalline* D_2O layers was estimated as $150 \pm 15 \text{ nm}$.

As shown in Fig. 5, a thin layer of D_2O , initially positioned at some distance away from the film surface, evolves from the ice film only after vaporization of the overlying H_2O^{16} layer. The time interval from the onset of H_2O vaporization to the appearance of the D_2O vaporization peak, or the mean residence time of D_2O in the bulk of the H_2O film, gives the mean reaction time for H/D isotopic exchange. Positioning the D_2O layer further away from the surface, i.e., increasing the mean reaction time, results in a gradual decrease of the magnitude of the D_2O peak. The decrease in the D_2O peak is accompanied by a gradual increase in the HDO yield, which signifies the rapid conversion of D_2O into HDO.

Figure 6 examines in detail the isothermal desorption spectra of D_2O and HDO resulting from a thin D_2O layer initially positioned 1000 nm away from the surface of a 3000 nm thick H_2O film. The isothermal desorption spec-

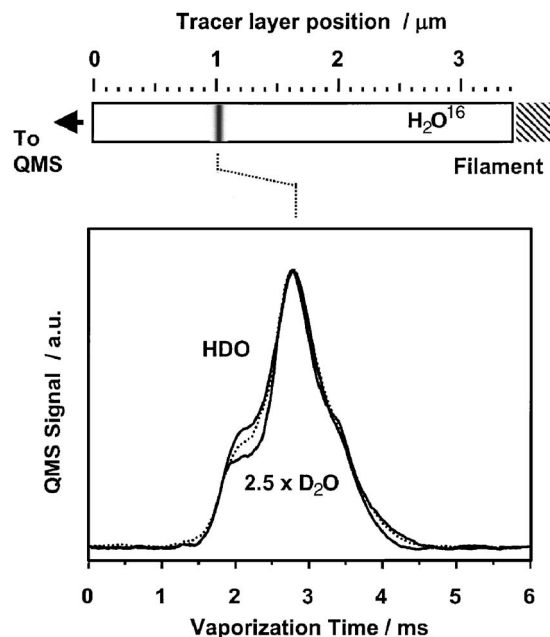


FIG. 6. Details of the isothermal desorption spectra of D_2O and HDO resulting from a thin D_2O layer initially positioned $1 \mu\text{m}$ away from the surface of a $3 \mu\text{m}$ thick H_2O^{16} film. The isothermal desorption spectrum of H_2O^{18} is shown for comparison. The initial thickness of the D_2O and H_2O^{18} layers was $60 \pm 10 \text{ nm}$. The desorption temperature was approximately -4°C . The zero on the time scale corresponds to the onset of H_2O^{16} desorption. As shown in the figure, the shapes of the HDO, D_2O , and H_2O^{18} spectra display significant similarities (see text for explanation of the spectrum features).

trum of H_2O^{18} is shown for comparison (dotted line). The initial thickness of D_2O and H_2O^{18} layers was $60 \pm 10 \text{ nm}$. The isothermal desorption temperature was -4°C . The zero on the time scale corresponds to the onset of H_2O desorption. As shown in the figure, the shapes of the HDO, D_2O , and H_2O^{18} spectra display significant similarities. The spectra are broad and consist of two distinct features: a shoulder at 2 ms and a peak at 2.8 ms . In our previous article,⁴¹ we provide a detailed explanation of the origin of the main features in the fast thermal desorption spectra. The essential conclusions are presented immediately below:

- (1) The shoulder in the isothermal desorption spectra of HDO, D_2O , and H_2O^{18} represents the vaporization of tracer species residing at or near the grain boundaries, whereas the peak corresponds to the vaporization of tracer species incorporated into the crystallites of the polycrystalline H_2O ice film.⁴¹
- (2) Diffusion of tracer species is much slower than the vaporization of the film. The shoulder in the vaporization spectra of HDO, D_2O , and H_2O^{18} is due to rapid vaporization of tracer molecules *trapped* at or near the grain boundaries. The peak is due to the release of tracer molecules trapped in the interior of the crystallites, which vaporize at a slightly slower rate compared to defect rich grain boundary regions of the film.⁴¹

The main goal of the experiments described in this article is to measure the diffusivity of HDO and D_2O molecules in polycrystalline H_2O^{16} ice, and thus to gain insights into the nature of the aqueous phase at grain boundaries.

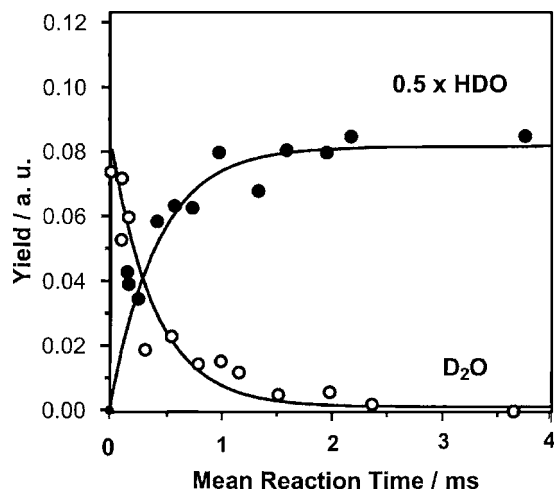


FIG. 7. The kinetics of the H/D exchange reaction in the case of an exceedingly thin (less than a few nanometers) D_2O layer. The yield values were calculated through integration of the isothermal desorption spectra of D_2O and HDO over vaporization time. The deuterium exchange between the D_2O layer and surrounding polycrystalline H_2O ice results in the nearly complete disappearance of D_2O on the time scale of a millisecond. A rapid decrease in the amount of unreacted D_2O is accompanied by a proportional increase in the HDO yield, which approaches its maximum value of approximately twice the initial amount of D_2O .

Although an analysis of the desorption spectra of H_2O ¹⁸ may, in principle, provide information on the diffusivity of the tracer species in the bulk of the polycrystalline H_2O ¹⁶ ice film, such an analysis would be complicated by the surface morphological dynamics of the ice films and by the time-of-flight broadening of the spectra associated with the 10 cm distance between the surface of the filament and the mass spectrometer.⁴¹ Nevertheless, as we will show in the following sections, studies of the H/D exchange kinetics between thin (10–300 nm) D_2O tracer layers and surrounding bulk H_2O still make it possible to gain quantitative information on water self-diffusivity in polycrystalline ice near its melting point.

B. H/D exchange kinetics

Figure 7 illustrates the kinetics of the H_2O+D_2O reaction in the case of an exceedingly thin D_2O layer. It shows the yield of D_2O and HDO as a function of mean reaction time. According to our best estimates, the initial thickness of the D_2O layer was less than a few nanometers. The vaporization temperature in these experiments was approximately $-2^\circ C$. The yield values were calculated through integration of the isothermal desorption spectra of D_2O and HDO over vaporization time. As shown in the figure, the deuterium exchange between the D_2O layer and surrounding polycrystalline H_2O ice results in near complete disappearance of D_2O on the time scale of a millisecond. A rapid decrease in the amount of unreacted D_2O is accompanied by a proportional increase in the HDO yield, which approaches its maximum value of approximately twice the initial amount of D_2O . Taking into account the small initial thickness of the D_2O layer, we arrive at the following important conclusion: when H/D isotopic exchange reaction is not limited by interdiffusion rate of D_2O and H_2O , the half-life of D_2O in the surrounding

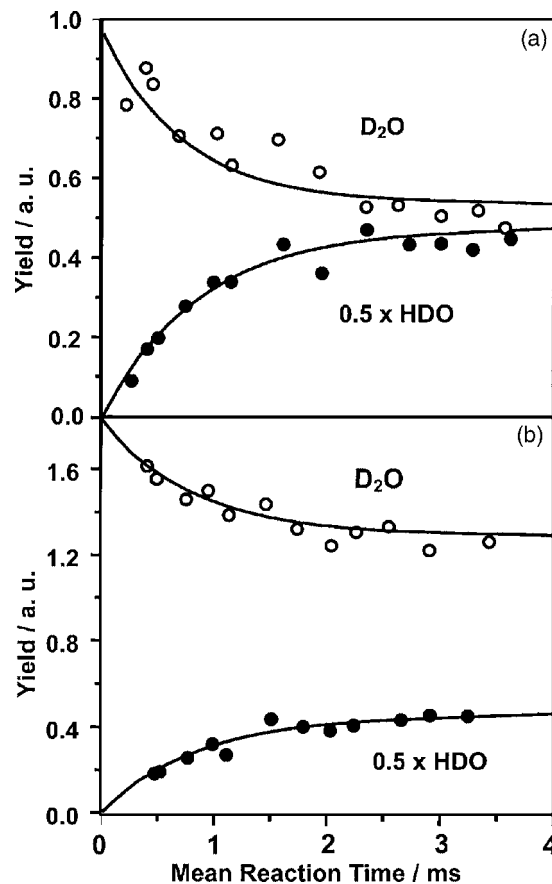


FIG. 8. Variations in the kinetics of the H/D exchange reaction with the initial thickness of the D_2O layer. (a) The initial thickness of the D_2O layer is approximately 100 nm. (b) The initial thickness of the D_2O layer is approximately 50 nm. While the HDO yield is nearly independent of the initial amount of D_2O , the increase in the initial D_2O layer thickness results in the proportional increase in the unreacted D_2O yield.

H_2O ice is near 1 ms. Such a short time of intermixing of D_2O and H_2O is consistent with the rate of self-diffusion even in single crystal ice ($D_c=10^{-6} \mu m^2/ms$).^{44–50}

Although the H_2O+D_2O reaction is nearly complete on the time scale of a millisecond in experiments with *ultrathin* D_2O layers, this is not the case with thicker deuterium oxide films. As shown in Fig. 8(b), when the layer's thickness is 50 ± 5 nm, only half of the initial D_2O layer is converted into HDO on the time scale of our experiment (4 ms). The fraction of D_2O that does *not* undergo isotopic exchange is even greater in the case of 100 ± 10 nm thick D_2O layers. As shown in Fig. 8(a), the increase in the D_2O layer thickness results in the proportional increase in the unreacted D_2O .

Figure 9 provides an explanation for the observed reaction kinetics. As shown in the figure, the H/D exchange is confined to a narrow reaction zone at the H_2O/D_2O interface which is defined by the rate of diffusive mixing between these species. Thus, the HDO yield, which is determined by the diffusivity of the D_2O in polycrystalline H_2O , must be independent of the initial thickness of the D_2O layer as long as the layer thickness exceeds the value equal to the width of the reaction zone. However, increasing the initial thickness of the D_2O layer must result in a *linear* increase in the D_2O yield. Indeed, when the initial thickness of the D_2O layer exceeds the width of the reaction zone, a fraction of the D_2O

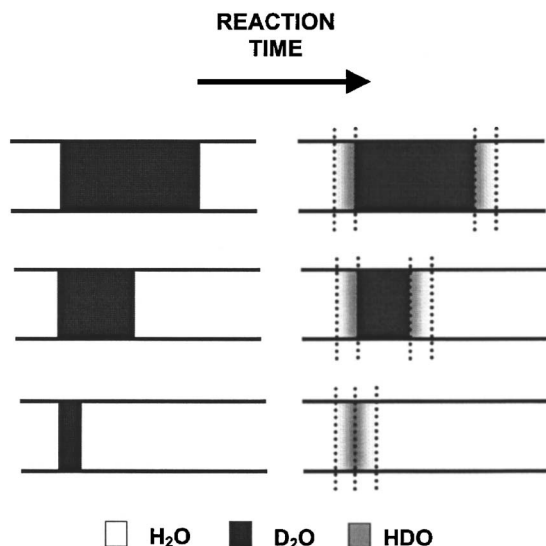


FIG. 9. Interpretation of the observed HDO and D₂O yield dependences on the initial thickness of the D₂O layer. The H/D exchange reaction must be confined to relatively narrow reaction zones at the interfaces between the pure H₂O and D₂O regions of the ice film. Thus, an increase in the initial amount of D₂O results in a proportional increase in the unreacted D₂O yield; however, the HDO yield is independent of the initial thickness of the D₂O layer. The widths of the reaction zones are defined by the characteristic scale of interdiffusion of H₂O and D₂O.

layer is unable to react with the surrounding H₂O due to insufficient extent of interdiffusion on the time scale of the FTDS experiment.

The interpretation of isotopic exchange kinetics given above is validated by an analysis of the HDO isothermal desorption spectra in the case of relatively thick (approximately 300 nm), initial D₂O layers. It follows from Fig. 9 that the HDO desorption spectrum resulting from a thick D₂O layer must be a superposition of desorption spectra of two thin HDO layers formed at the reaction zones on *both sides* of the D₂O slab. Thus, the HDO desorption spectrum resulting from a thick D₂O layer must be nearly identical to the HDO desorption spectrum resulting from *two* thin D₂O layers separated by a distance equal to the width of the thick D₂O layer.

Figure 10 compares the HDO desorption spectra in the case of a thick (300 nm) initial D₂O layer and in the case of two thin (50 nm) D₂O layers separated by a distance of 250 nm. In both cases the spectra were measured at approximately -2°C . As shown in the top panel of Fig. 10, the thick D₂O layer results in a HDO spectrum which is much broader than a typical HDO spectrum in the case of a single thin D₂O layer. Nevertheless, as shown in the lower panel of Fig. 10, its shape can be easily approximated as a simple sum of two HDO spectra from two thin D₂O layers, which are separated by a distance in the H₂O matrix.

C. Effective width of the reaction zone

As we already stated, the width of the reaction zone for the H/D exchange must be determined by the rate of interdiffusion of H₂O and D₂O in polycrystalline ice. Thus, if the width of the reaction zone is known, the self-diffusivity of water in polycrystalline ice can be estimated using character-

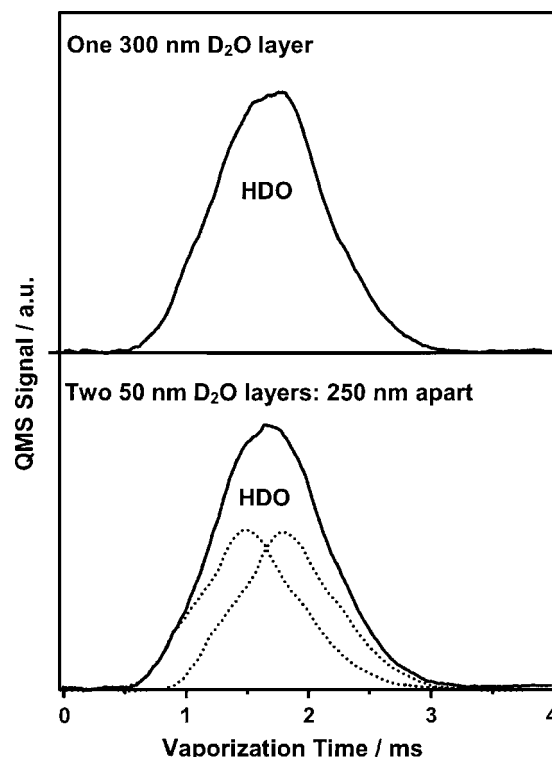


FIG. 10. Top panel: Fast thermal desorption spectrum of HDO resulting from a 300 nm thick D₂O layer in a 3 μm thick H₂O film. The spectra were measured at approximately -2°C . The D₂O layer was positioned 1000 nm away from the film's surface. Lower panel: A simulated fast thermal desorption spectrum of HDO from two 50 nm thick D₂O layers separated by a H₂O layer of 250 nm (solid line). The similarities between the measured and the simulated spectra support our conclusion that H/D exchange reaction is confined to two narrow reaction zones at the interfaces between the H₂O and D₂O regions in the ice films.

istic time of the experiment. In this section, we describe a procedure which we used to infer the width of the reaction zone. We begin with assuming that the H₂O/D₂O/H₂O films have the simple geometry illustrated in Fig. 9. Taking into account the geometry of the film, the thickness of the D₂O layer, $L_{\text{D}_2\text{O}}(t_R)$, at any moment, t_R , during reaction can be approximated as

$$L_{\text{D}_2\text{O}}(t_R) \approx L_{\text{D}_2\text{O}}(0) - L_{\text{RZ}}(t_R), \quad (1)$$

where $L_{\text{D}_2\text{O}}(0)$ is the initial thickness of the D₂O layer, and L_{RZ} is the width of the diffusion-limited reaction zone. Note that Eq. (1) only applies when the initial thickness of the D₂O layer is greater or equal to the width of the reaction zone. Assuming that D₂O and HDO yields must be proportional to the thickness of the D₂O layer and the width of the reaction zone, respectively, their ratio can be calculated at any moment of time during the reaction as

$$\frac{\text{D}_2\text{O}^{\text{yield}}}{\text{HDO}^{\text{yield}}}(t_R) \approx \chi \left[\frac{L_{\text{D}_2\text{O}}(0)}{L_{\text{RZ}}(t_R)} - 1 \right], \quad (2)$$

where χ is a numeric factor. According to Eq. (2), the ratio of the D₂O and HDO yields increases *linearly* with the initial thickness of the D₂O layer as long as the initial thickness is greater than the width of the reaction zone at t_R . Furthermore, the ratio of D₂O and HDO yields approaches zero

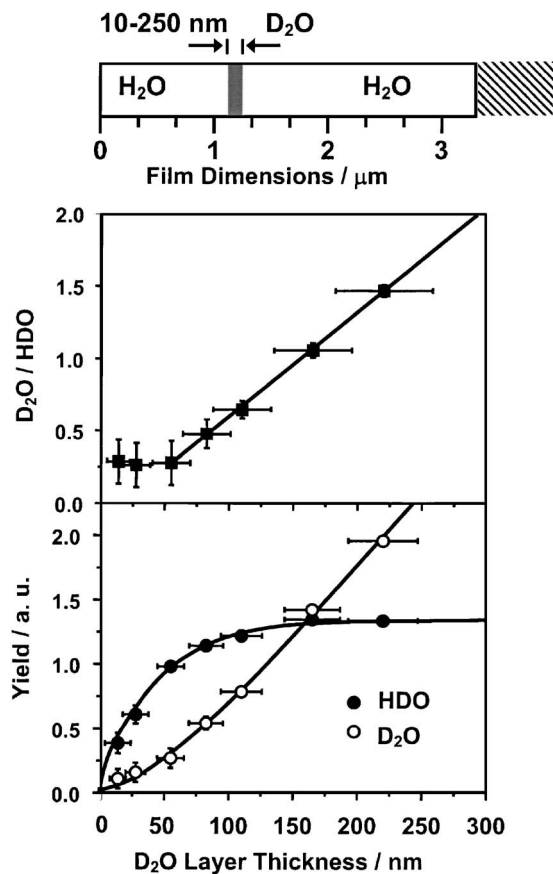


FIG. 11. Dependence of HDO and D₂O yields on the initial thickness of the D₂O layer. The yields correspond to the mean reaction time of 3 ms. The desorption temperature was approximately -2°C . In agreement with Eq. (2), the ratio of the D₂O and HDO yields increases linearly with initial D₂O layer thickness when it is greater than 50 nm. According to the interpretation of the reaction kinetics illustrated in the previous figure, this value represents the width of the reaction zone after reaction time of 3 ms.

when the initial thickness of the D₂O layer is equal to the width of the reaction zone at t_R . In short, the width of the reaction zone can be estimated in a reaction-desorption experiment, where the initial thickness of the D₂O layer is varied in a systematic fashion.

Figure 11 shows the result of such a study. The data in the upper panel represent the experimentally determined ratio of the HDO and D₂O yields as a function of the initial thickness of the D₂O layer. The yields correspond to the mean reaction time t_R of 3 ms. The temperature in these experiments was $-2 \pm 1^{\circ}\text{C}$. As shown in the figure, the ratio of the D₂O and HDO yields increases linearly with an initial D₂O layer thickness when the D₂O layer thickness is greater than 50 nm. Thus, we conclude that for H/D exchange reaction between polycrystalline D₂O and H₂O layers at $-2 \pm 1^{\circ}\text{C}$, the width of the reaction zone approaches 50 ± 25 nm at $t_R = 3$ ms. Because the dimensions of the reaction zone must be governed by the interdiffusivity of H₂O and D₂O, the width of the reaction zone is essentially the diffusive interpenetration depth at the interface of polycrystalline D₂O and H₂O ice. In the following sections, we will use this result to infer the value of the self-diffusion coefficient along the GB's in polycrystalline ice and to gain insight into the extent of GB premelting at temperatures near 0°C .

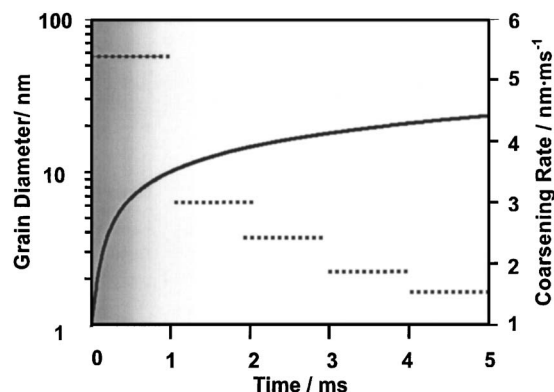


FIG. 12. The grain dimensions and growth kinetics in the polycrystalline ice films expected under the conditions characteristic of our FTDS experiments. Because polycrystalline ice films are formed by rapid crystallization of initially amorphous deposits and because the time scale of a typical FTDS is short, the resulting average grain size is likely to be less than 30 nm.

IV. DISCUSSION

A. Crystallite dimensions and transport properties

Over the past 40 years, diffusion of various chemical species in polycrystalline materials has been the focus of numerous theoretical studies, which have produced reliable, experimentally verified methods for characterization of chemical transport along the grain boundaries.⁵¹⁻⁵⁶ These methods typically require at least some quantitative knowledge of the morphology of polycrystalline material under consideration. Thus, in order to complete the theoretical interpretation of the result of the diffusion/reaction experiments described in the previous sections of this article, we must, first, obtain an estimate of the average size of the grains in our polycrystalline ice samples.

As we have already stated, our FTDS experiments commence with the deposition of an amorphous H₂O/D₂O/H₂O film at temperatures near -153°C . During rapid heating, this amorphous film spontaneously crystallizes in the temperature range of -50 to -20°C . After crystallization, the film must undergo a process of grain coarsening. In general, the kinetics of this process can be described by the following equation:⁵⁷

$$G_t^n - G_0^n = k(T)t, \quad (3)$$

where n is the grain growth exponent ($n \geq 2$), G_t is the average effective grain diameter, G_0 is the initial grain diameter, and $k(T)$ is the temperature dependent grain growth constant.

When the grain growth is uninhibited, the growth exponent is close to 2. Impurities and voids, such as air bubbles, in the bulk of a polycrystalline sample tend to slow down the coarsening process, therefore increasing the value of the growth exponent in Eq. (3). The grain growth constant, $k(T)$, has been measured in the past for polycrystalline ice samples of various morphology and chemical composition. A comprehensive review of these data can be found in Ref. 57. Using this extensive information on the kinetics of grain growth in polycrystalline ice, we can gain estimates of the average grain size typical for our experimental conditions.

Figure 12 shows the grain growth kinetics in polycrys-

talline ice films in our FTDS experiments. The average grain diameter was calculated according to Eq. (3) with the grain growth exponent equal to 2 and using the grain growth rate constant of $49 \text{ nm}^2/\text{ms}$ at $-2 \text{ }^\circ\text{C}$.^{57,58} Because polycrystalline ice in our experiments is formed by rapid crystallization of mostly amorphous ice, we assume that the initial average diameter of the crystallites is on the order of several molecular diameters. We also note that the grain growth constant value used to generate data in Fig. 12 is one of the greatest observed at temperatures near ice melting point and corresponds to bubble-free, impurity-free polycrystalline ice.^{57,58} Because our ice samples may contain voids, which are formed as a result of the collapse of low-density microporous amorphous ice during rapid heating,⁴² the data in Fig. 12 must be interpreted as the *upper* estimate of the average grain diameter. As shown in Fig. 12, the average diameter of the crystallites during isothermal vaporization near $0 \text{ }^\circ\text{C}$ is on the order of 10–30 nm.

In addition to the grain diameter values, the graph in Fig. 12 also shows estimates for the average velocities of grain boundary motion at various stages of the experiment. The motion of the grain boundaries is the inevitable result of grain ripening. As we will explain in the following sections, the grain boundary motion velocity is an important parameter in interpreting the data from the diffusivity experiments.

Another key parameter for the interpretation of the results of our H/D exchange experiments is water self-diffusion coefficient in the interior of the crystallites. Because grain dimensions in our polycrystalline ice samples may be as small as a few nanometers, the diffusion coefficient of water and other species in such microscopic ice single crystals may differ from those in bulk single crystal ice. Livingston *et al.* have shown that self-diffusivity of water in thin (few tens of nanometers) films may exceed that in the bulk samples by almost two orders of magnitude.⁵⁹ Extrapolating this result to the temperatures near ice melting point, we obtain a value of $10^{-4} \mu\text{m}^2/\text{ms}$ for the estimate of the upper limit of water diffusivity in our nanocrystallites. The lower limit for the diffusion coefficient in microscopic crystallites at $-2 \text{ }^\circ\text{C}$ is given by the value of water self-diffusion coefficient in defect-free bulk ice single crystals that is on the order of $10^{-6} \mu\text{m}^2/\text{ms}$.^{45–50} In summary, we assume the following values for the properties of the microscopic grains in our polycrystalline ice samples:

- (1) The average grain diameter is between 10 and 30 nm.
- (2) The water self-diffusion coefficient in the crystallites is between 10^{-6} and $10^{-4} \mu\text{m}^2/\text{ms}$ at $-2 \text{ }^\circ\text{C}$.
- (3) The average velocity of the grain boundary motion is between 0 and 3 nm/ms.

B. Water diffusivity along grain boundaries

Our analysis of water self-diffusivity along the grain boundaries relies on the estimate of the width of the reaction zone, which is determined by the rate of intermixing of D_2O and H_2O at the interface of two isotopically distinct regions in polycrystalline ice. In other words, our experimental arrangement is essentially a diffusion couple, where the char-

acteristic *penetration depth* is essentially the width of the reaction zone. The penetration depth L may be a function of the following parameters: the diffusion coefficient at the grain boundaries, D_{gb} , the diffusion coefficient in the crystallites, D_c , the average crystallite size G , the grain boundary width δ , and the “annealing time” t , which is the average reaction time for H/D exchange in our FTDS experiments. A particular relationship between L and the other variables depends on the relative magnitudes of D_{gb} , D_c , G , δ , and t .^{51,60–62}

In the case of stationary boundaries, three regimes of diffusion can be distinguished in polycrystalline materials. The conditions, which give rise to these distinct diffusion kinetics and the corresponding relationships between the penetration depth and other parameters, are listed immediately below.

(1) *C regime.* The C regime arises when the characteristic diffusion scale in the crystallites is significantly smaller than a typical grain boundary width, i.e., when

$$(D_c t)^{1/2} \ll \delta, \quad D_c < D_{\text{gb}}. \quad (4)$$

In this case, the penetration depth is determined primarily by the diffusivity along the grain boundaries and can be estimated using the following simple equation:

$$L \approx (D_{\text{gb}} t)^{1/2}. \quad (5)$$

(2) *B regime.* The B regime occurs when the characteristic diffusion scale in the crystallites is much greater than the grain boundary width but much smaller than the average crystallite diameter, i.e., when

$$\delta \ll (D_c t)^{1/2} \ll G, \quad D_c < D_{\text{gb}}. \quad (6)$$

In the B regime, L is defined by the diffusion coefficient at the grain boundaries, D_{gb} , and in the crystallites, D_c , as well as by the width of the grain boundaries, L can be estimated using the following equation:

$$L \approx (\delta D_{\text{gb}})^{1/2} (t/D_c)^{1/4}. \quad (7)$$

Note that although Eq. (7) was originally derived for the case of a single boundary between two infinite crystallites, it was later shown that it gives a good (within an order of magnitude) estimate of the penetration depth in the case of diffusion through a three-dimensional network of intersecting grain boundaries as long as condition (6) is satisfied.^{51,62,63}

(3) *A regime.* The A regime emerges when the characteristic diffusion scale in the crystallites is much greater than the average diameter of the crystallites, i.e., when

$$G \ll (D_c t)^{1/2}, \quad D_c < D_{\text{gb}}. \quad (8)$$

In this case, L can be related to the parameters of the polycrystalline material by the following equation:

$$L \approx (\varepsilon_c D_c t + \varepsilon_{\text{gb}} D_{\text{gb}} t)^{1/2}, \quad (9)$$

where ε_c and ε_{gb} are the volume fractions of crystallites and grain boundaries in the bulk of a polycrystalline material, respectively. The volume fractions can be estimated as

$$\varepsilon_{\text{cr}} \approx G/(G + \delta), \quad (10)$$

$$\varepsilon_{gb} \approx \delta/(G + \delta), \quad (11)$$

where G and δ are the usual average grain diameter and the grain boundary width. Note that the expression enclosed in parentheses in Eq. (9) is essentially D_{eff} , where D_{eff} , the effective diffusion coefficient, is given by the Hart-Mortlock equation,^{51,64,65} i.e., by a linear combination of diffusion coefficient along the grain boundaries and the diffusion coefficient in the crystallites.

Rearranging terms in Eqs. (5), (7), and (9), we obtain expressions which make it possible to calculate the diffusion coefficient along the grain boundaries as a function of other parameters for different diffusive regimes:

$$D_{gb} \approx L^2/t \quad (C \text{ regime}), \quad (12)$$

$$D_{gb} \approx \frac{L^2 D_c^{1/2}}{\delta t^{1/2}} \quad (B \text{ regime}), \quad (13)$$

$$D_{gb} \approx \frac{L^2}{t} \left(\frac{G}{\delta} + 1 \right) - \frac{G}{\delta} D_c \quad (A \text{ regime}). \quad (14)$$

Note that Eq. (14) cannot give a negative value for the diffusion coefficient along the grain boundaries because under no physically meaningful conditions can the diffusivity in crystallites, D_c , exceed the term L^2/t . Indeed, in the A regime, the penetration depth L is determined by a linear combination of the diffusion coefficients within the crystallites and along the grain boundaries [see Eq. (9)]. Thus, L is always equal to or greater than $(D_c t)^{1/2}$ as long as $D_c < D_{gb}$.

Equations (12)–(14) make it possible to estimate D_{gb} under a variety of experimental conditions. Before proceeding with the analysis, we must discuss restrictions on applying these relationships under these conditions characteristic of our measurements. As emphasized by Eqs. (5), (6), and (8), Eqs. (12)–(14) assume that the grain boundary diffusivity is greater than the diffusivity in the crystallites. More important, Eqs. (12)–(14) were derived for the case of stationary boundaries.⁶⁰ However, as shown in Fig. 11 the grains in our polycrystalline ice films may undergo some degree of growth, which results in moving grain boundaries.

The perturbations to the concentration profiles of diffusing species due to the movement of the grain boundaries constitute a reduction of the penetration depth L .^{51,66} This effect can be explained by a more efficient trapping of the diffusing species by the crystallites.^{51,62,67} Thus, if grain boundary motion is not taken into account, estimates of the grain boundary diffusivity may give a value of the diffusion coefficient along the grain boundaries that is significantly lower than the actual value. The error in the calculations of D_{gb} , due to grain boundary motion, is defined by the ratio γ of the boundary displacement to the characteristic diffusion distance in the crystallites during the time of the experiment:^{51,66}

$$\gamma = \frac{V_{gb} t}{(D_c t)^{1/2}}, \quad (15)$$

where V_{gb} is the average velocity of GB motion. We note that under the conditions of our FTDS experiments, γ is unlikely to be significantly greater than unity. Indeed, even assuming

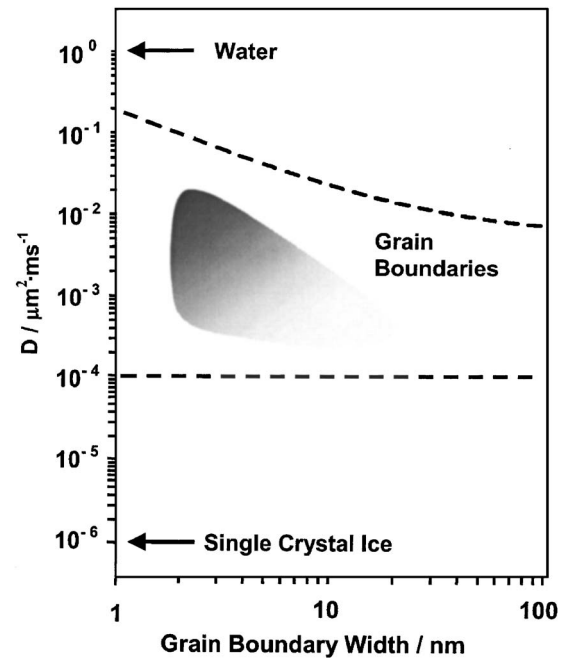


FIG. 13. The range of the water self-diffusion coefficients along the grain boundaries and the grain boundary widths, which are consistent with the inferred dimensions of the reaction zone for the H/D isotopic exchange in polycrystalline ice. The diffusion coefficients of H₂O in liquid water and in single crystal ice are shown for comparison. The dotted lines represent the upper and lower estimates of the self-diffusion coefficient. The lowest, physically meaningful width of the grain boundaries is assumed to be 1 nm or approximately two water monolayers. The shaded region shows the range of the most likely values of the diffusion coefficients and grain boundary widths.

the lowest value of D_c ($10^{-6} \mu\text{m}^2/\text{ms}$) and the maximum value of grain boundary velocity (3 nm/ms), we obtain a γ value that is approximately 5.

An estimate of D_{gb} in the case of moving grain boundaries can be derived simply as

$$D_{gb}^{\text{true}} \approx \frac{1}{2} \gamma D_{gb}^{\text{apparent}} \quad (16)$$

where D_{gb}^{apparent} is the grain boundary diffusion coefficient determined without taking into consideration possible motion of the grain boundaries.^{51,66} According to Eq. (16), the grain boundary migration is unlikely to result in a significant (more than an order of magnitude) correction factor for calculations of D_{gb} under our experimental conditions. Nonetheless, in order to obtain the upper estimate of D_{gb} , we will assume that the maximum value of diffusivity along the grain boundaries is an order of magnitude higher than those given by Eqs. (12)–(14).

Although many parameters of the diffusion in our polycrystalline ice films are *not* precisely defined, we can still use Eqs. (11)–(14) to infer the range of possible D_{gb} and δ values, which are consistent with the maximum penetration depth inferred from H/D exchange experiments (50 nm). The results of this analysis are shown in Fig. 13. The diffusion coefficients of H₂O in bulk liquid water and in bulk single crystal ice are shown for comparison. The upper dotted line is given by Eq. (14), which corresponds to the A diffusive regime. The lowest, physically meaningful width of the grain boundaries is assumed to be 1 nm, or approxi-

mately two to three water monolayers. We note that the self-diffusion coefficient along the grain boundaries, D_{gb} , approaches a maximum ($0.1 \mu\text{m}^2/\text{ms}$) when the grain boundary width δ is at its minimum. This general relationship between D_{gb} and δ must be obeyed in any theoretical treatment of diffusion in polycrystals as long as the diffusivity at grain boundaries is greater than that in the crystallites. Indeed, increasing the volume fraction of a component with a high diffusion coefficient in the composite material must ultimately lead to increase in the overall rate of diffusive transport.

The data summarized in Fig. 13 lead to an important conclusion: The 50 nm length scale of diffusive transport observed in our H/D exchange experiments is inconsistent with waterlike diffusivity of H_2O and D_2O along grain boundaries in fine polycrystalline ice samples near their melting point. Although grain boundaries serve as conduits for rapid diffusion, the values of the H_2O and D_2O self-diffusion coefficient along the grain boundaries are likely to be a few orders of magnitude lower than those in bulk liquid water even near 0°C . In the following section, we examine the implications of this result for possible grain boundary phase transitions.

C. Grain boundary premelting in the limit of low concentrations of impurities

The estimates of the upper limits of water self-diffusivity described in the previous section make it possible to derive important conclusions about the extent of premelting at the grain boundaries and related defect at temperatures a few degrees below bulk melting point of ice. Before proceeding, the terminology relevant to the premelting phenomena must be discussed.

As already mentioned, interfacial melting or premelting of ice consists in the formation of thin (nanometer scale) liquid layers at various single crystal ice interfaces, i.e., at the interface between ice and vapor, ice and another solid, or ice and a liquid (other than water) at temperature below ice melting point. Such thin layers are often referred to as quasi-liquid or liquidlike layers, which, by itself, reflects the fact that the properties of aqueous phase formed as a result of interfacial premelting are still not completely understood. For example, Wei *et al.* postulated the “onset of surface melting” at temperatures as low as -75°C . They based this conclusion on results of sum frequency generation (SFG) spectroscopy measurements, which might have been sensitive to variations in hydrogen bonding primarily in the top ice bilayer.⁶⁸ While clearly demonstrating that ice surface becomes progressively more disordered with increasing temperature, it is unclear if these SFG results show unambiguously the existence of waterlike film on ice.

We note that the current theoretical description of premelting implies the formation of a liquid layer with properties, such as surface tension, similar to those of bulk water.^{35–39} Therefore, we emphasize that by premelting at the grain boundaries, we mean the formation of a liquid layer, which is at least a few water monolayers thick and the molecular transport properties of which are similar to those in

bulk water. In other words, we define premelting as the onset of waterlike diffusivity of H_2O and D_2O along grain boundaries with the width of *at least* 1 nm. In the light of the definition given above, the conclusion of our study is straightforward: When the concentrations of impurities are low, the grain boundary premelting is unlikely at temperatures below $-2 \pm 1^\circ\text{C}$. This conclusion is in agreement with theoretical analysis of grain boundary premelting by Benatov and Wettlaufer, who argue that premelting at temperatures a few degrees below melting point requires a substantial concentration of ionic impurities at the grain boundaries.³⁹

V. SUMMARY AND CONCLUSIONS

Using the FTDS approach, we were able to obtain detailed information on the kinetics of the H/D exchange reaction in polycrystalline $\text{H}_2\text{O}/\text{D}_2\text{O}/\text{H}_2\text{O}$ ice films at temperatures near ice melting point. According to our results, the isotopic exchange between H_2O and D_2O was confined to a narrow (approximately 50 nm) reaction zone at the interface between two isotopes of polycrystalline ice. Taking into account a typical time scale of our experiments and the likely crystallite dimensions and crystallite diffusivities, we were able to infer the range of values for the water self-diffusion coefficients and grain boundary dimensions consistent with the observed H/D reaction kinetics. These data indicate that, in the case of low concentrations of impurities, grain boundary premelting is implausible at temperatures as high as -2°C . Thus, the results of this study provide experimental support to recent theoretical analysis of grain boundary phase transitions.

The experiments describe in this article also demonstrate that the FTDS approach is well suited for studies of reaction kinetics in thin films of volatile polycrystalline solids. Furthermore, we show that by combining our FTDS technique with precision deposition of ultrathin films, it is possible to gain quantitative information on the nanoscale molecular transport in these experimentally challenging condensed phase systems.

ACKNOWLEDGMENTS

We would like to thank the participants of 11th International Conference on Physics and Chemistry of Ice for insightful comments on the details of this work. We also gratefully acknowledge the support from the National Science Foundation (Grant No. 0416091) that made this study possible.

¹J. S. Wettlaufer, in *Physics of Ice-Covered Seas*, edited by M. Leppranta (University of Helsinki Press, Helsinki, 1998).

²J. W. Glen, D. R. Homer, and J. G. Paren, *Int. Assoc. Sci. Hydrol.*, Publ. n62 **118**, 263 (1977).

³J. G. Dash, *Science* **246**, 1591 (1989).

⁴A. W. Rempel and M. G. Worster, *J. Cryst. Growth* **223**, 420 (2001).

⁵M. G. Worster and J. S. Wettlaufer, in *Fluid Dynamics at Interfaces*, edited by W. Shyy and R. Narayanan (Cambridge University Press, Cambridge, 1999).

⁶H. P. Marshall, J. T. Harper, W. T. Pfeffer, and N. F. Humphrey, *Geophys. Res. Lett.* **29**, 2146 (2002).

⁷D. L. Goldsby, in *Glacier Science and Environmental Change*, edited by P. Knight (Blackwell, Malden, MA, 2006).

⁸W. F. Weeks, in *Physics of Ice-Covered Seas*, edited by M. Leppranta

- (University of Helsinki Press, Helsinki, 1998), pp. 25–104.
- ⁹ P. B. Black, *Historical Perspectives of Frost Heave Research, Historical Perspectives in Frost Heave Research: The Early Works of S. Taber and G. Beskow*, edited by P. B. Black and M. J. Hardenberg, CRREL Special Report No. 91-23 (CRREL, Hanover, NH, 1991), p. 37.
- ¹⁰ R. Bindschadler, *Science* **282**, 428 (1998).
- ¹¹ C. R. Bentley, *Science* **275**, 1077 (1997).
- ¹² M. Oppenheimer, *Nature* (London) **393**, 325 (1998).
- ¹³ National Academy of Science, *Sea-Level Change* (National Academy Press, Washington, DC, 1990).
- ¹⁴ R. Zhang, M.-T. Leu, and M. Molina, *Geophys. Res. Lett.* **23**, 1669 (1996).
- ¹⁵ K. S. Carslaw and T. Peter, *Geophys. Res. Lett.* **24**, 1743 (1997).
- ¹⁶ R. Halde, *Nuovo Cimento Soc. Ital. Fis., A* **14**, 575 (1980).
- ¹⁷ B. Chalmers, *Sci. Am.* **200**(2), 114 (1959).
- ¹⁸ W. M. Elmore, "Water purification by natural freezing," M.Sc. thesis, University of Wyoming, 1968.
- ¹⁹ A. A. Chernov and A. M. Mel'nikova, *Sov. Phys. Crystallogr.* **10**, 672 (1966).
- ²⁰ A. W. Rempel, E. D. Waddington, J. S. Wettlaufer, and M. G. Worster, *Nature* (London) **411**, 568 (2001).
- ²¹ V. Sadtchenko, M. Brindza, M. Chonde, B. Palmore, and R. Eorn, *J. Chem. Phys.* **121**, 11980 (2004), and references therein.
- ²² I. Baker, D. Cullen, and D. I. Liescu, *Can. J. Phys.* **81**, 1 (2003).
- ²³ V. F. Petrenko and R. W. Whitworth, *Physics of Ice* (Oxford University Press, Oxford, 1999).
- ²⁴ P. V. Hobbs, *Ice Physics* (Clarendon, Oxford, 1974).
- ²⁵ J. S. Wettlaufer, *Interface Sci.* **9**, 115 (2001).
- ²⁶ J. S. Wettlaufer, *Philos. Trans. R. Soc. London, Ser. A* **357**, 3403 (1999).
- ²⁷ F. E. Livingston, J. A. Smith, and S. M. George, *J. Phys. Chem. A* **106**, 6309 (2002).
- ²⁸ V. Sadtchenko, G. E. Ewing, D. R. Nutt, and A. J. Stone, *Langmuir* **18**, 4632 (2002).
- ²⁹ W. Kuhn and M. Thürkau, *Helv. Chim. Acta* **41**, 938 (1958).
- ³⁰ Y. Mizuno and N. Hanafusa, *J. Phys. Colloq.* **48**, 511 (1987).
- ³¹ S. Mantovani, S. Valeri, A. Loria, and U. del Pennino, *J. Chem. Phys.* **72**, 1077 (1980).
- ³² S. J. Johnsen, H. B. Clausen, W. Dansgaard, N. S. Gundestrup, C. U. Hammer, U. Andersen, K. K. Andersen, C. S. Hvidberg, D. Dahl-Jensen, J. P. Steffensen, H. Shoji, A. E. Sveinbjörnsdóttir, J. White, J. Jouzel, and D. Fisher, *J. Geophys. Res.* **102**, 26397 (1997).
- ³³ J. F. Nye, *J. Glaciol.* **44**, 467 (1998).
- ³⁴ S. J. Johnsen, H. B. Clausen, K. M. Cuffey, G. Hoffmann, J. Schwander, and T. Creyts, in *Physics of Ice Records*, edited by T. Hondoh (Hokkaido University Press, Sapporo, 2000).
- ³⁵ J. G. Dash, in *Ice Physics and the Natural Environment*, NATO Advanced Studies Institute, Series I: Global Environment Change, edited by J. S. Wettlaufer, J. G. Dash, and N. Untersteiner (Springer, New York, 1999), vol. 56, pp. 11–22.
- ³⁶ J. G. Dash, H. Y. Fu, and J. S. Wettlaufer, *Rep. Prog. Phys.* **58**, 115 (1995).
- ³⁷ J. S. Wettlaufer, *Philos. Trans. R. Soc. London, Ser. A* **357**, 1 (1999).
- ³⁸ J. G. Dash, A. W. Rempel, and J. S. Wettlaufer, *Rev. Mod. Phys.* **78**, 695 (2006).
- ³⁹ L. Benatov and J. S. Wettlaufer, *Phys. Rev. E* **70**, 061606 (2004).
- ⁴⁰ V. Sadtchenko and G. E. Ewing, *J. Chem. Phys.* **116**, 4686 (2002).
- ⁴¹ H. P. Lu, S. A. McCartney, M. Chonde, D. Smyla, and V. Sadtchenko, *J. Chem. Phys.* **125**, 044709 (2006).
- ⁴² For review, see R. A. Baragiola, in *Water in Confining Geometries*, Springer Series in Cluster Physics Vol. XII, edited by V. Buch and J. P. Devlin, (Springer, Berlin, 2003), pp. 359–395.
- ⁴³ Y. P. Handa, O. Mishima, and E. Whalley, *J. Chem. Phys.* **84**, 2766 (1986).
- ⁴⁴ F. E. Livingston, G. C. Whipple, and S. M. George, *J. Phys. Chem. B* **101**, 6127 (1997).
- ⁴⁵ O. Dengel and N. Riehl, *Phys. Kondens. Mater.* **1**, 191 (1963).
- ⁴⁶ K. Itagaki, *SIPRE Res. Rep.* **178**, 14 (1966).
- ⁴⁷ K. Itagaki, *J. Phys. Soc. Jpn.* **22**, 427 (1967).
- ⁴⁸ H. Blinks, O. Dengel, and N. Riehl, *Phys. Kondens. Mater.* **4**, 375 (1966).
- ⁴⁹ P. Delibaltas, O. Dengel, D. Helmreich, N. Riehl, and H. Simon, *Phys. Kondens. Mater.* **5**, 166 (1966).
- ⁵⁰ R. O. Ramseier, *J. Appl. Phys.* **38**, 2553 (1967).
- ⁵¹ I. Kaur, Y. Mishin, and W. Gust, *Fundamentals of Grain and Interphase Boundary Diffusion* (Wiley, Chichester, 1995).
- ⁵² I. Kaur, W. Gust, and L. Kozma, *Handbook of Grain and Interphase Boundary Diffusion Data* (Ziegler, Stuttgart, 1989).
- ⁵³ N. L. Peterson, *Int. Met. Rev.* **28**, 65 (1983).
- ⁵⁴ D. Gupta, D. R. Campbell, and P. S. Ho, in *Thin Films: Interdiffusion and Reactions*, edited by J. M. Poate, K. N. Tu, and J. W. Mayer (Wiley, New York, 1978), p. 161.
- ⁵⁵ G. Martin and B. Perrailon, in *Grain Boundary Structure and Kinetics*, edited by R. W. Balluffi (American Society of Metals, Metals Park, OH, 1980), p. 239.
- ⁵⁶ G. R. Purdy, *Defect Diffus. Forum* **83**, 131 (1992).
- ⁵⁷ O. Nasello and L. Arena, *Physics and Chemistry of Ice*, edited by N. Maeno and T. Hondoh (Hokkaido University Press, Hokkaido, 1992), pp. 422–427.
- ⁵⁸ L. Arena, O. B. Nasello, and L. Levi, *J. Phys. Chem. B* **101**, 6109 (1997).
- ⁵⁹ F. E. Livingston, G. C. Whipple, and S. M. George, *J. Chem. Phys.* **108**, 2197 (1998).
- ⁶⁰ L. G. Harrison, *Trans. Faraday Soc.* **57**, 1991 (1961).
- ⁶¹ Y. M. Mishin and C. Herzig, *Nanostruct. Mater.* **6**, 859 (1995).
- ⁶² A. D. Le Claire, *Br. J. Appl. Phys.* **14**, 351 (1963).
- ⁶³ J. C. Fisher, *J. Appl. Phys.* **22**, 74 (1951).
- ⁶⁴ E. W. Hart, *Acta Metall.* **5**, 597 (1957).
- ⁶⁵ A. J. Mortlock, *Acta Metall.* **8**, 132 (1960).
- ⁶⁶ Y. M. Mishin and I. M. Razumovskii, *Acta Metall. Mater.* **40**, 839 (1992).
- ⁶⁷ A. M. Glaeser and J. M. Evans, *Acta Metall.* **34**, 1545 (1986).
- ⁶⁸ X. Wei, P. B. Miranda, and Y. R. Shen, *Phys. Rev. Lett.* **86**, 1554 (2001).